ADVANCED FUNCTIONAL MATERIALS
www.afm-journal.de

Materials Views
www.MaterialsViews.com

Nanofragmentation of Ferroelectric Domains During Polarization Fatigue

*Hanzheng Guo, Xiaoming Liu, Jürgen Rödel, and Xiaoli Tan**

The microscopic mechanism for polarization fatigue in ferroelectric oxides has remained an open issue for several decades in the condensed matter physics community. Even though numerous models are proposed, a consensus has yet to be reached. Since polarization reversal is realized through ferroelectric domains, their behavior during electric cycling is critical to elucidating the microstructural origin for the deteriorating performance. In this study, electric field in situ transmission electron microscopy is employed for the first time to reveal the domain dynamics at the nanoscale through more than 10^3 cycles of bipolar fields. A novel mechanism of domain fragmentation is directly visualized in polycrystalline $[(Bi_{1/2}Na_{1/2})_{0.95}Ba_{0.05}]_{0.98}La_{0.02}TiO_3$. Fragmented domains break the long-range polar order and, together with domain wall pinning, contribute to the reduction of switchable polarization. Complimentary investigations into crystal structure and properties of this material corroborate our microscopic findings.

1. Introduction

Fatigue degradation of ferroelectric materials has been a vexing issue for both fundamental science and technological applications.[1–7] It is manifested primarily in the form of continuous reduction in switchable polarization upon repeated electric cycling,[2,8,9] which has stood out as the primary hindrance to high reliability and long service life of ferroelectric devices, such as non-volatile memories, field-effect transistors, ferroelectric tunneling junctions, transducers and actuators.[1–9] To elucidate the underlying mechanisms for the performance deterioration, phenomenological and theoretical studies have been extensively conducted on ferroelectric thin films and bulk materials.[2,8–11] Despite these efforts, the origin of polarization fatigue still remains controversial, and various models have been proposed, including passive layer formation,[12] nucleation inhibition,[13] local phase decomposition,[14] near-by-electrode injection,[8] defect redistribution,[15] and domain wall pinning.[16] Since polarization fatigue is a complicated defect-chemistry phenomenon, one single mechanism alone cannot explain all the observations.[8] Some fatigue characteristics are always conjugated with each other. For example, the widely observed domain wall pinning mechanism is always accompanied with charge injection[17] or nucleation inhibition features.[18]

The vast majority of previous fatigue studies has focused on the evolution of macroscopic properties against electric cycling, such as permittivity, remanence, and coercivity.[2,7–9,19] The microscopic dynamics is then indirectly inferred from the change of property. It should be noted that the polarization state and polarization reversal are intrinsically linked to ferroelectric domain arrangement and its transformation. Under externally applied electric field, ferroelectric domains adjust their configuration through domain wall motion and they eventually dictate the macroscopic properties.[20] The domain activities occur at a length scale ranging from nanometers to micrometers.[20,21] To better elucidate the domain dynamics and its role on polarization degradation during fatigue, direct microscopic imaging of domain evolution becomes essential. As such, a few studies have been reported in the literature, which employed piezoresponse force microscopy (PFM)[17,18,22–26] and synchrotron X-ray microdiffraction27 to visualize domains mostly on thin films of classic ferroelectrics, such as $BiFeO_3$ and $Pb(Zr,Ti)O_3$. Although these probing tools can produce micrographs, they are still challenged by some technical limitations. For example, PFM only monitors the domain morphology change without providing any crystallographic information. It is well known that an electric field can induce structural phase transitions which can be detected by electron diffraction.[20,21] However, it will be difficult for PFM to distinguish subtle differences between the phase variants in perovskite ferroelectrics. For the X-ray microdiffraction, the spatial resolution is around several micrometers.[27] Even with the recent development of submicrometer X-ray diffraction, higher resolution is still quite challenging, especially when individual grains with multiple domains are concerned. To circumvent these technical constraints and unravel the microstructural origin of polarization fatigue, the electric field in situ transmission electron microscopy (TEM) technique[28–33] is employed in the present study.

We report the first in situ TEM investigation on polarization fatigue in a lead-free piezoelectric ceramic. Polycrystalline ceramic of $[(Bi_{1/2}Na_{1/2})_{0.95}Ba_{0.05}]_{0.98}La_{0.02}TiO_3$ (BNT52) was chosen for its nonergodic relaxor nature and high piezoelectric property.[34] The evolution of domains within individual grains under applied electric fields was directly observed at high

Dr. H. Z. Guo, Mr. X. Liu, Prof. X. Tan
Department of Materials Science and Engineering
Iowa State University
Ames, IA 50011, USA
E-mail: xtan@iastate.edu
Prof. J. Rödel
Institute of Materials Science
Technische Universität Darmstadt
Darmstadt 64287, Germany

DOI: 10.1002/adfm.201402740

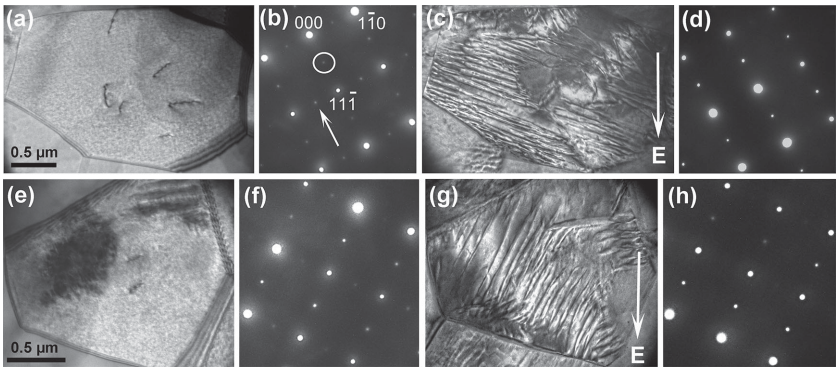

Figure 1. In situ TEM observations on domain and phase evolution during initial poling in BNT52. a) Bright field micrograph of a grain along its [112] zone axis in virgin state, and b) the corresponding electron diffraction pattern prior to initial poling. c) Bright field micrograph and d) electron diffraction pattern of the same grain as in (a) at a nominal field of 30 kV cm^{-1}. e) Bright field image of another [112]-aligned grain, and f) the corresponding electron diffraction pattern in the virgin state. g) Bright field image and h) electron diffraction pattern of the same grain as in (e) at a nominal field of 30 kV cm^{-1}. The directions of the applied fields in the in situ TEM experiment are indicated by the bright arrows in (c) and (g) respectively. The ½{*ooo*} and ½{*ooe*} superlattice diffraction spots are highlighted by a bright circle and a bright arrow, respectively, in (b).

resolution. The nanodomains in the virgin state transformed to large lamellar domains during the first quarter cycle of field through a phase transition; these large domains were disrupted gradually during bipolar electric cycling; and finally much less responsive domain fragments were formed. Correspondingly, such domain fragmentation process yielded a logarithmic reduction of switchable polarization. The multistep process of 180° polarization reversal model is suggested to account for the observed domain fragmentation during bipolar fatigue.[22]

2. Results and Discussion

2.1. Domain and Phase Evolution During Initial Poling

Prior to cycling, the evolution of domain morphology during the very first quarter cycle of electric field (referred to as "initial poling" hereafter) was examined and is displayed in **Figure 1**. As demonstrated previously, BNT52 is a non-ergodic relaxor in its virgin state.[34] As displayed in Figure 1a of a representative grain along its [112] zone axis, it consisted of nanometer-sized domains with coexisting *R3c* and *P4bm* phases, revealed by the weak ½{*ooo*}- and ½{*ooe*}-type (*o* and *e* stand for odd and even Miller indices, respectively) superlattice electron diffraction spots (Figure 1b), respectively.[35–37] Unlike the dynamically fluctuating polar nanoregions in ergodic relaxors,[38,39] the static polar nanodomains shown in Figure 1a can be irreversibly switched during initial poling.[21] Figure 1c provides the stable domain morphology at 30 kV cm^{-1}, the original nanodomains are consumed by long lamellar ferroelectric domains with the development of long-range polar order. Crystallographic analysis indicates that the major set of domain walls are parallel to the {010} planes. At the same time, this domain morphology transformation was accompanied by a *P4bm* to *R3c* symmetry change, as indicated by the disappearance of the ½{*ooe*} superlattice spots and the significantly strengthened ½{*ooo*} ones (Figure 1d). Such microstructural change was repeatedly observed, as exemplified by another [112]-aligned grain (Figure 1e–h), and was found irreversible. Both the domain morphology alteration (Figure 1c,g) and crystal structural transition (Figures 1d and 1h) remained unchanged after the applied field is removed.

2.2. Domain Fragmentation During Bipolar Electric Cycling

The large lamellar domains formed during initial poling were found to be disrupted by subsequent bipolar electric cycling, as demonstrated in **Figure 2** on a [112]-aligned grain. The major set of walls of the induced lamellar domains (Figure 2a) are along the {110} crystallographic plane while the selected area electron diffraction pattern (inset of Figure 2c) suggests an *R3c* symmetry. After 20 cycles of bipolar electric fields of nominal intensity of 30 kV cm^{-1}, the domain morphology of this grain was significantly altered. The well-aligned lamellar domains were replaced by other sets of large domains (Figure 2b). It is interesting to notice that large domains were fragmented and small domains appeared in the central portion of the grain. The disruption of large domains continued and

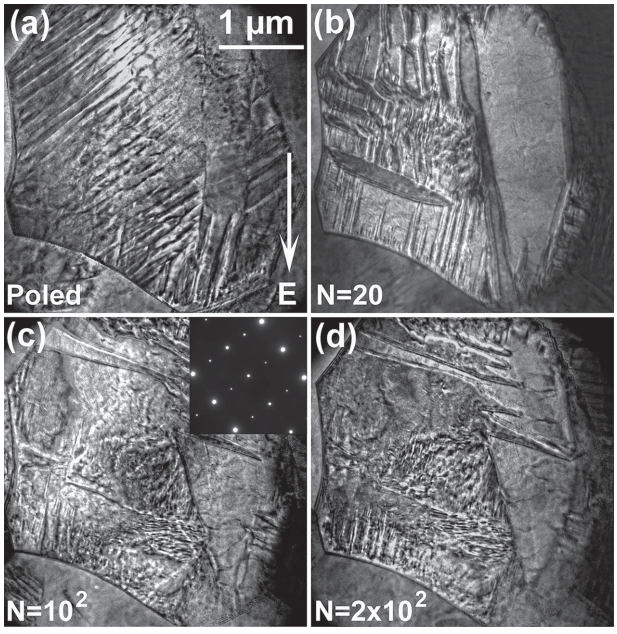

Figure 2. Evolution of ferroelectric domains during bipolar electric cycling of BNT52. Bright field micrographs of a [112]-aligned grain a) the initially poled state at 30 kV cm^{-1} prior to cycling; b) after 20; c) 10^2; and d) 2×10^2 cycles of bipolar electric fields. The electron diffraction pattern of the poled state is shown as the inset in (c). No apparent changes in the diffraction pattern were observed during cycling. The positive direction of applied fields in the in situ TEM experiment is indicated by the bright arrow in (a).

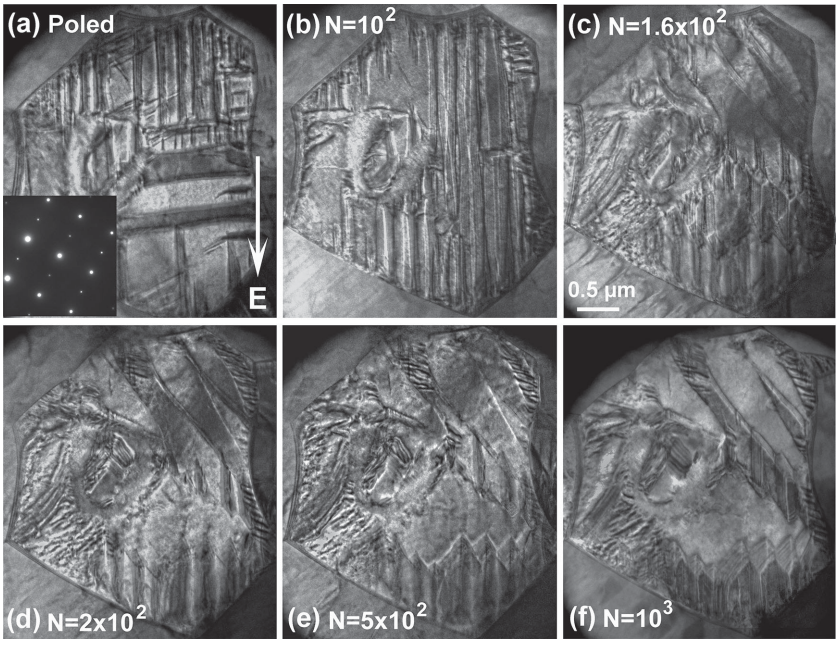

Figure 3. Evolution of ferroelectric domains during bipolar electric cycling in another [112]-aligned grain in the same TEM specimen as in Figure 2. Bright field micrographs of a) the initially poled state at 30 kV cm^{-1} prior to cycling; b) after 10^2; c) 1.6×10^2; d) 2×10^2; e) 5×10^2; and f) 10^3 cycles of bipolar electric fields. The electron diffraction pattern of the initially poled state is shown as the inset in (a). No noticeable changes in the diffraction pattern were observed during bipolar cycling. The positive direction of applied fields in the in situ TEM experiment is indicated by the bright arrow in (a).

gradually spread to the most part of the grain during further bipolar cycling (Figure 2c,d). It was also observed that domains in some areas became stable and less responsive to the electric stimulus. After 2×10^2 cycles (Figure 2d), nearly a third of the grain was occupied by nanometer-sized domain fragments. Additionally, after the initially poling no noticeable changes were found in the electron diffraction patterns during bipolar cycling.

The domain fragmentation during bipolar electric cycling was corroborated in the same TEM specimen, as exemplified by another [112]-aligned grain provided in **Figure 3**. Again, large lamellar domains with *R3c* symmetry were developed during the initially poling (Figure 3a). After 10^2 cycles of electric cycling, the morphology of the large domains changed dramatically (Figure 3b). When the cycling number reached 1.6×10^2, a large portion of lamellar domains in the central left part of the grain was perturbed by the emergence of condensed domain clusters (Figure 3c). Upon further bipolar cycling (Figures 3d–f), more domain fragments were observed with an increased domain wall density; meanwhile the domain walls were gradually pinned and became less mobile during cycling. After 10^3 cycles (Figure 3f), the switching ability of the domains was significantly suppressed, and eventually a configuration with mixed domain fragments and immobile large domains was resulted. Again, the electron diffraction pattern of the grain after initial poling stayed unchanged during the course of bipolar cycling.

The domain fragmentation during bipolar electric cycling occurs in grains with different crystallographic orientations as well. **Figure 4** reveals the process observed in a [111]-aligned grain in the same TEM specimen. A microstructural evolution similar to that in Figure 2,3 was seen again. After initial poling, large lamellar domains with walls along $\{01\bar{1}\}$ planes were observed (Figure 4a). It should be noted that the weak contrast of domain walls in the left part of the grain was due to bend contours. The [111] zone-axis diffraction pattern (Figure 4b) from this grain after initial poling indicates the absence of ½{*ooe*}-type superlattice spots, which is consistent with the results from other grains shown in Figure 1–3. During bipolar electric cycling, the large lamellar domains were continuously disrupted into small fragments. This can be clearly seen from Figures 4d–g, as well as from the corresponding higher magnification micrographs displayed in Figures 4h–j. After 10^3 cycles (Figure 4g), the great majority of the grain was occupied by small domain fragments. The fragmented domain configuration persisted to higher numbers of electric cycling. Compared with those grains depicted in Figure 2,3, the domain fragmentation in this grain is more thorough and extensive. This difference seems to indicate an orientation dependence of the fragmentation process during bipolar cycling. In addition, after 10^3 cycles, the difference also gives rise to the crystallographic variance since both fragmentations and large domains contribute to the electron diffraction patterns. It is most interesting to see that the ½{*ooe*} superlattice diffraction spots seem to re-appear in the electron diffraction pattern after 10^3 cycles (Figure 4c). However, they were not found in the [112] zone-axes electron diffraction patterns shown in Figure 2, 3, which could be due to the incomplete fragmentation process. The results indicate that the bipolar electric cycling not only disrupts the large *R3c* domains, but also has a tendency to recover the *P4bm* phase. In other words, the electric cycling seems to gradually transform the microstructure after initial poling back to the original nanodomains in the virgin state. We have recently demonstrated that the polarization reversal in this composition takes place through complicated phase transitions,[40] indicating close free energies of those variant phases. The accumulated and redistributed charged point defects, such as oxygen vacancies, during bipolar electric cycling may destabilize the long range ordered ferroelectric state (in the form of large *R3c* domains) and favor the short range ordered relaxor state (in the form of *R3c* and *P4bm* nanodomains). However, the extremely weak ½{*ooe*} spots indicate that the fatigued specimen was still dominated by the *R3c* phase.

It should be made clear that the observed domain fragmentation is not likely due to the thermal depolarization, which occurs at a temperature slightly below 50 °C in the studied composition.[34] During the in situ TEM experiment, to avoid possible temperature increase in the ceramic specimen, a very low frequency of 1 Hz of the applied bipolar cyclic field was used

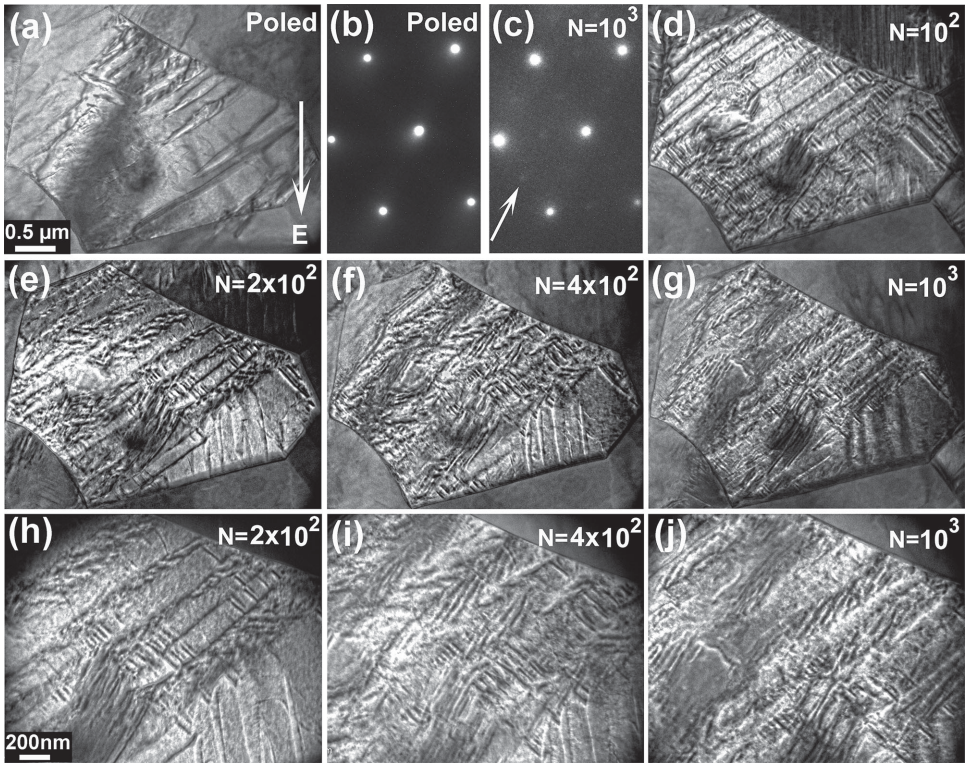

Figure 4. Domain fragmentation during bipolar electric cycling revealed by in situ TEM observations on a [111]-aligned grain in the same TEM specimen as in Figure 2, 3. a) Bright field micrographs, and b) the corresponding electron diffraction pattern, of the initially poled state at 30 kV cm^{-1} prior to cycling. c) Electron diffraction pattern from the same area after 10^3 cycles of bipolar fields. The ½{*00ε*}-type superlattice diffraction spots can be barely seen and are indicated by the bright arrow. The fragmentation of large lamellar domains during bipolar cycling is shown by the bright field micrographs, d) after 10^2; e) 2×10^2; f) 4×10^2; and g) 10^3 cycles of applied field. Higher magnification images of (e,f,g) are shown in (h,i,j), respectively. The positive direction of applied fields in the TEM experiment is indicated by the bright arrow in (a).

and the grain of interest was always moved away from electron beam illumination during cycling. In addition, the fatigue test was carried out 100 cycles at a time. TEM observations made after each 100 cycles and at the end of the cyclic test indicated no temperature-induced changes in domain morphology and diffraction patterns.

The domain fragmentation process during electric cycling was found to be accompanied by the immobilization of domains walls in all grains displayed in Figures 2–4. Let us utilize the grain featured in Figure 4 as illustrative example. After 10^3 cycles of bipolar electric cycling, the domain morphology provided in Figure 4g did not change under a nominal DC field of 30 kV cm^{-1} in both polarities, suggesting that most domains were frozen. When a higher DC field of 40 kV cm^{-1} was applied, those immobilized domain walls started to move and a different domain morphology was resulted (**Figure 5**). Long and thin domains were formed in the central and upper-middle portions of the grain, as well as large domains grew in the lower part of the grain. However, compared with the domain morphology after the initial poling depicted in Figure 4a where only large lamellar domains were present, the morphology after fatigue shown in Figure 5 contains a much higher domain wall density. Apparently the domain wall mobility is significantly suppressed by the electric cycling and the electric poling becomes much less effective even under a higher field of 40 kV cm^{-1}.

2.3. Impact on Macroscopic Structure and Properties

To ensure that the in situ TEM result is representative for the behavior of bulk ceramics, X-ray diffraction measurements on a bulk specimen were performed. As revealed by the in situ TEM results (Figure 1), the ½{*000*}-type superlattice diffractions,

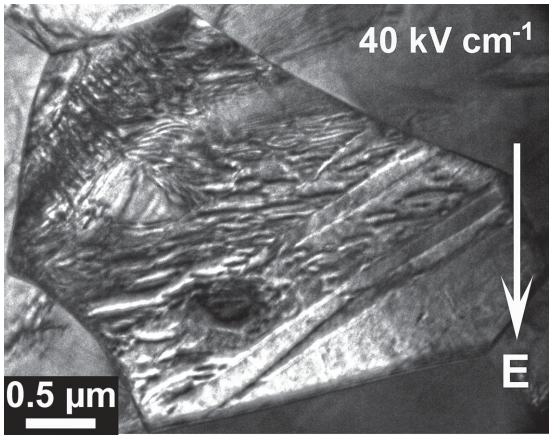

Figure 5. The frozen domains after fatigue. Bright field micrograph of the domain morphology under a nominal DC field of 40 kV cm^{-1} after 1.2×10^3 cycles in the same grain as in Figure 4. The direction of the DC field is indicated by the bright arrow.

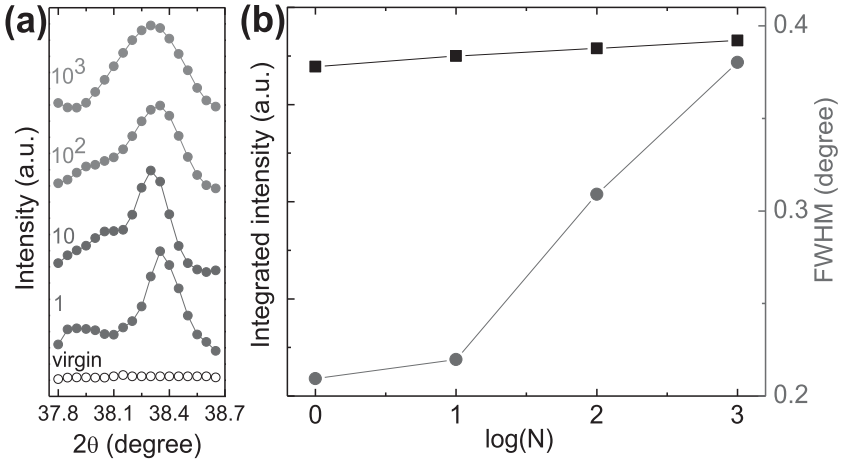

Figure 6. Domain size reduction during bipolar electric cycling demonstrated in a bulk BNT52 ceramic specimen. a) Evolution of the ½(311) superlattice diffraction peak monitored by X-ray diffraction at different cycling numbers. b) Integrated peak intensity and the full width of half maximum (FWHM) of the ½(311) peak as a function of the cycling number.

characteristic of the ferroelectric *R3c* phase,[35–37] displayed dramatic changes after electric field exposure. Therefore, the evolution of the ½(311) superlattice diffraction peak was monitored during bipolar electric cycling of the bulk specimen.

In the virgin state prior to exposure of any electric field, the ½(311) peak was too weak to be detected by the conventional laboratory X-ray diffractometer (**Figure 6**a). However, an apparent and sharp ½(311) peak was detected after the first cycle of bipolar electric fields. The superlattice peak persisted but gradually became broad during the subsequent electric cycling. Figure 6b displays the integrated intensity and the full width of half maximum (FWHM) of the ½(311) peak against the cycling number. It is evident that the peak intensity remains almost constant while the FWHM is almost doubled after 10^3 cycles.

The broadening of X-ray diffraction peaks is often indicative of a reduction of the average domain size. For example, during the pressure-induced phase transition in bulk CdSe, nanodomain fragmentation yields an apparent broadening of the diffraction peaks.[41] Therefore, the X-ray diffraction analysis of the bulk BNT52 specimen correlates well with the in situ TEM results shown in Figure 2–4. The *R3c* phase, either in the form of large domains or domain fragments, was overwhelmingly predominant during bipolar electric cycling. However, the large domains decompose into fragments with increased electric reversals. An oversimplified estimate using the Debye-Scherrer equation gives an average domain size of 40 nm after the first electric cycle and 22 nm after 10^3 cycles. These values seem reasonable for the width of domains from TEM observations.

Microstructural changes inevitably give rise to alterations of macroscopic properties. **Figure 7** depicts the evolution of the polarization and strain hysteresis loops with increasing cycling numbers. The irreversible relaxor to ferroelectric transition revealed by the in situ TEM (Figure 1) is verified by the abrupt development of large polarization and strain during the first quarter cycle of electric field as well as the presence of remanence after initial poling. Upon increase in cycling numbers, the polarization loops became depressed with a continuous reduction of maximum and switchable polarizations (P_m and P_r), but an increase in coercive field E_C (**Figure 8**a). Quantitatively, P_m and P_r feature a similar degradation of 35% and 32% from their original values after 1.5×10^4 cycles, respectively; while E_C jumps to 155% of its initial value. Meanwhile, the positive strain (the maximum strain on the x_{33} versus E loops) deteriorates moderately and the negative strain (the minimum strain on the x_{33} vs E loops) shifts toward zero after the first cycle (Figure 8b).

For classic ferroelectrics, such as Pb(Zr,Ti)O_3 and $BiFeO_3$, their fatigue behavior usually exhibits a nonlinear three-stage decay of remanent polarization when plotted against the logarithm of electric reversals,[9] an initial slow stage ($N \sim 10^4$), a logarithmic stage ($N \sim 10^6$), and a saturated stage ($N \sim 10^8$). The obtained fatigue profiles are generally fitted

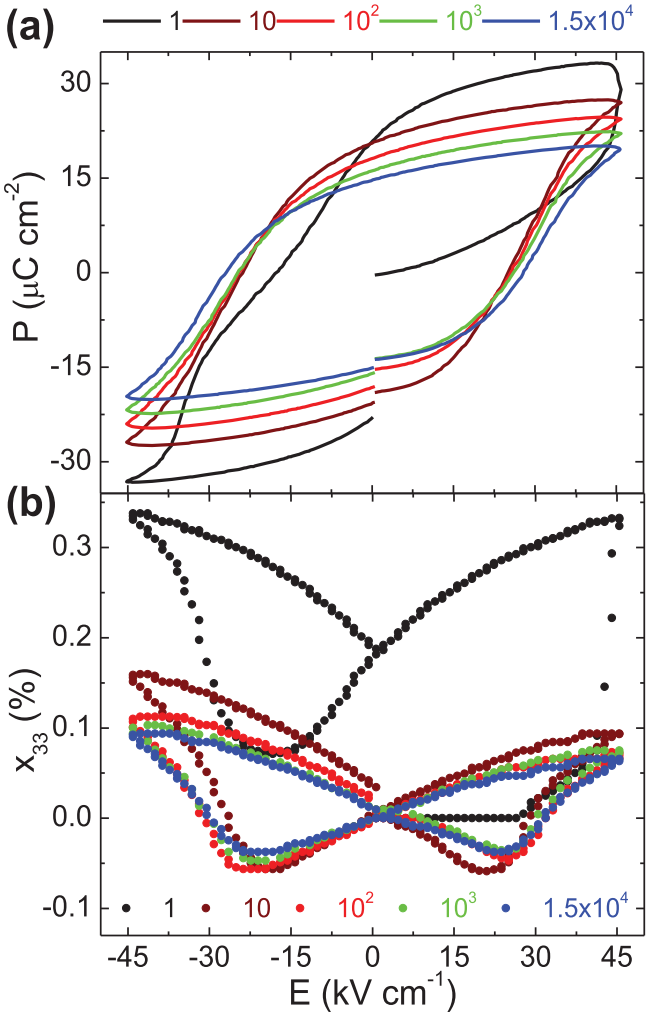

Figure 7. Fatigue effect on hysteresis loops in a bulk BNT52 specimen. Evolution of a) polarization, P, and b) longitudinal strain, x_{33}, hysteresis during fatigue.

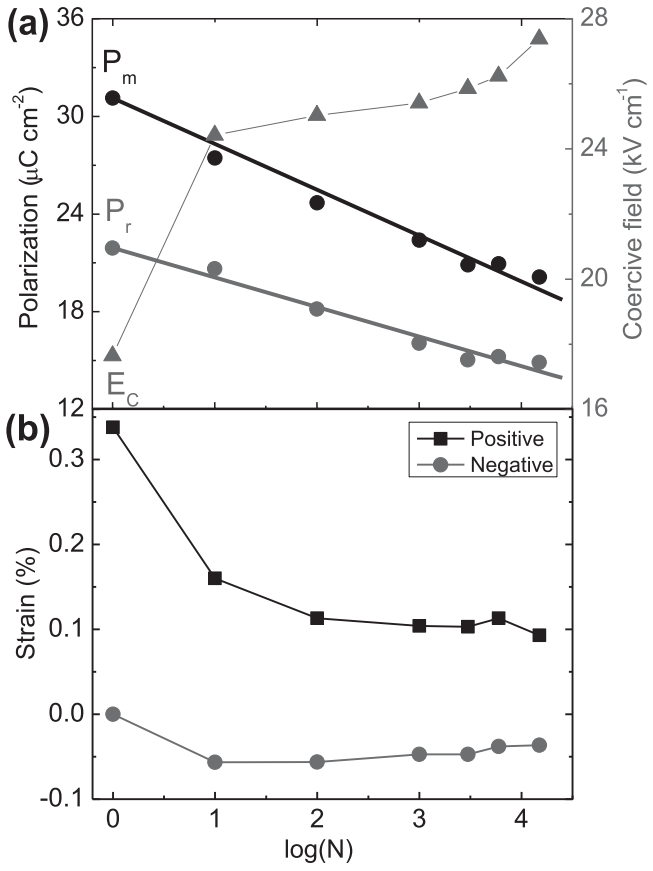

Figure 8. Evolution of the key macroscopic properties during fatigue. a) Evolution of the maximum polarization, P_m, remanent polarization, P_r, and coercive field, E_C, against cycling number N. b) Evolution of the longitudinal strain at the maximum (positive) and minimum (negative) points of the strain hysteresis loops. All discrete points are experimentally measured values and their error bars are of the order of the size of symbols and not shown. The straight solid lines in (a) for P_m and P_r are the fitting curves for the equations presented in the text.

by functions like $P_r \propto N^{-}1/4$, $P_r \propto (aN+1)^{-m}$, or $P_r \propto A+exp(-aN)$ (Refs. [8,42]). In contrast, the BNT52 ceramic in the present study displayed a nearly linear polarization decay right from the beginning in the semi-log plot, as provided in Figure 8a. The polarization degradation, both P_r and P_m, can be well fitted by the logarithmic fatigue relation proposed by Brennan:[43]

$$P = P_0 + A\log(N) \quad (1)$$

where P_0 is the polarization prior to fatigue; N is the cycle number; and A is a rate factor and can be expressed as (kT/c) with k the Boltzmann constant, T the temperature, and c a proportionality constant. The fitting equations for P_r and P_m are

$$P_r = 21.9 - 1.8\log(N) \quad (2)$$

$$P_m = 31.1 - 2.8\log(N) \quad (3)$$

respectively. The rate factor A characterizes the speed of polarization decay during fatigue. Apparently, it depends on the chemical composition, as well as fatigue conditions. In a ceramic with a similar composition of $[(Bi_{1/2}Na_{1/2})_{0.94}Ba_{0.06}]TiO_3$, a much greater $A \approx -9.9$ μC/cm^2 was observed within the first 10^4 cycles of bipolar sinusoidal fields of 60 kV cm^{-1} at 2 Hz.[44] La-addition in the present study has slowed down the polarization deterioration.

2.4. Discussion

It is commonly accepted that polarization fatigue is a defect-chemistry induced phenomenon in ferroelectrics of both thin film and bulk forms.[2,8] Complicated processes are involved during electric cycling, primarily including the creation and/or redistribution of charged defects which subsequently influence the ferroelectric domain switching dynamics.[2,8] Also, the initially charge-neutral domain walls can become polarized during electric reversal, which will enhance their interactions with defects.[17,22] In a word, the resulting fatigue effect is generally due to the formation of mesoscopic structures of interacting charged defects and polarized walls.[43] It has been shown that ionic defects may produce a self-trapping potential by polarizing the surrounding crystal lattice, leading to an increase in the activation energy for defects in the mesoscopic structures.[43] As a system, the charged defects and polarized domain walls form a self-stabilizing configuration through charge compensation.[2,17,22,43] For example, oxygen vacancies, the most mobile defects in perovskite oxides, aggregate at the tail-to-tail domain walls to compensate the negative charges; meanwhile the electrons accumulate at the head-to-head charged domain walls to neutralize the positive polarization charges.[17,22] Such interactions result in domain wall pinning and nucleation inhibition through deactivating domain switching events. All these microscopic processes contribute to the logarithmic decay of the switchable polarization upon electric cycling.[43]

In the BNT52 ceramic reported here, charged defects can be oxygen vacancies, aliovalent substituting cation, or vacancies of Bi and Na cations due to evaporation loss during sintering. Also, extrinsic contribution from electrode injection cannot be ruled out when prolonged cycling is considered.[17] Since fatigue in BNT52 commenced at the very beginning (Figure 7,8) and a progressively freezing domain configuration was reached before 10^3 cycles (Figure 2–4), we suggest a predominant role of the intrinsically produced charge defects instead of injected ones. The interactions between these charged defects and domain walls yield a stabilized and freezing domain configuration revealed by the in situ TEM observation. In addition to domain wall pinning, a novel phenomenon of domain fragmentation was confirmed in this study. As noticed in Figure 2–4, most of the domain fragments were distorted without a preferential crystallographic plane for their walls, suggesting they were not charge neutral.[22] The formation of such fragments with charged domain walls can be well-understood with assistance of the multistep process of 180° polarization reversal model.[22]

Various experimental evidences have verified that the 180° polarization reversal in rhombohedral ferroelectric perovskites [e.g., $BiFeO_3$, $Pb(Zn_{1/3}Nb_{2/3})O_3$-$PbTiO_3$, and $Pb(Mg_{1/3}Nb_{2/3})$

O_3-$PbTiO_3$] is accomplished through consecutive non-180° ferroelastic domain switching instead of the straightforward reverse.[22,45–49] $BiFeO_3$, possessing the same *R3c* space group as the poled BNT52, was found to form charged domain walls through the multistep switching process.[22] Moreover, both experimental observations and theoretical calculations revealed that the 71° polarization switching in $(Bi_{1/2}Na_{1/2})TiO_3$, the base compound of BNT52, was the dominant pathway for the electric field-induced polarization switching since the energy barrier for the 71° switching was much lower than those for the 109° switching and 180° reversal.[50] Therefore, the 180° switching (e.g., $[111] \rightarrow [\bar{1}\bar{1}\bar{1}]$) can be realized through three intermediate steps of 71° ferroelastic switching upon electric field reversal.[22] There exist six different equivalent routes for this reversal and two of them are exemplified below:

$$\text{Route 1 (R1)}: [111] \xrightarrow{1st} [\bar{1}11] \xrightarrow{2nd} [\bar{1}\bar{1}1] \xrightarrow{3rd} [\bar{1}\bar{1}\bar{1}]$$

$$\text{Route 2 (R2)}: [111] \xrightarrow{1st} [11\bar{1}] \xrightarrow{2nd} [1\bar{1}\bar{1}] \xrightarrow{3rd} [\bar{1}\bar{1}\bar{1}]$$

In ideal situations, there is no energetic preference among the six routines.[22] Therefore, polarization switching in a rhombohedral crystal will follow any of the six routes and experience all the intermediate states with equal probability during electric reversal. In this process, there is a large chance for the formation of charged domain walls when two different intermediate domains meet, for example, the conjunction of $[\bar{1}11]$ in R1 and $[11\bar{1}]$ in R2, or $[\bar{1}\bar{1}1]$ in R1 and $[1\bar{1}1]$ in R2. Presumably, the charged walls are unfavorable due to their high electrostatic energy. However, they can be stabilized by trapping mobile charge carriers, leading to pinned domain walls with reduced mobility. As the reversal repeated over and over again, more and more intermediate domains with frozen domain walls will be accumulated. This explains the domain fragmentation and polarization degradation upon bipolar electric cycling. It should be noted that Simons et al. speculated a domain fragmentation process during bipolar electric cycling based on their neutron diffraction data from bulk ceramic specimens of a related composition of $[(Bi_{1/2}Na_{1/2})_{0.94}Ba_{0.06}]TiO_3$.[51] After 10^3 cycles, their neutron diffraction pattern from the fatigued specimen becomes indistinguishable from the virgin specimen, with no evidence of peak splitting, broadening or poling texture. In the present work, the nanofragmentation of ferroelectric domains during polarization fatigue is directly observed for the first time with the in situ TEM technique in a modified composition of BNT52.

Another complication during bipolar electric cycling in the present BNT52 is phase transition. BNT52 is a non-ergodic relaxor with a thermal depolarization temperature T_d slightly above room temperature.[34] As depicted in Figure 1, there is an electric field-induced relaxor to ferroelectric phase transition during the first quarter cycle of electric field and the induced ferroelectric phase is maintained in the second quarter cycle. We recently observed that the initial relaxor phase could be partially recovered when the field reversed polarity in the third quarter cycle.[40] Therefore there are four phase transitions within a full cycle of bipolar electric fields and this is the cause for the pinched polarization hysteresis loop for cycle 1 shown in Figure 7a. However, the recovery of the relaxor phase seems to vanish during the subsequent cycling as the distortions on the hysteresis loops disappear. The very weak ½{*ooe*} superlattice spots in the fatigued specimen (Figure 4c) suggests the presence of a very minor amount of the relaxor phase. It appears that the subtle balance between the relaxor *R3c* and *P4bm* phases and the ferroelectric *R3c* phase is slightly changed by fatigue generated species, such as charged point defects and high-density domain walls. In other words, the fatigue process alters the energy landscape of different phases, which in turn, changes the phase transition pathway.

Lastly, it should be pointed out that other factors may also have contributed to the polarization fatigue of BNT52, including electrode degradation, near-electrode passive layers, cycling-induced microcracks, and internal bias field from charge-accumulation at grain boundaries.[2,8,9,52] Since these phenomena occur at length scales longer than the grain size, they are beyond the primary interest of the present in situ TEM study.

3. Conclusions

In summary, in situ TEM was employed for the first time to investigate the domain structure evolution during electric fatigue in a non-ergodic lead-free relaxor BNT52. Complementary to the domain wall pinning effect, a novel fatigue mechanism of domain fragmentation was verified. The fragmentation was suggested to result from the frozen intermediate domains for the 180° polarization reversal. The pinned domain fragments led to the reduction of switchable polarization through destruction of long-range polar order. These direct nanoscale observations correlate very well with the performance deterioration seen on bulk specimens and hence broaden the current understanding of the polarization fatigue mechanisms.

4. Experimental Section

The $[(Bi_{1/2}Na_{1/2})_{0.95}Ba_{0.05}]_{0.98}La_{0.02}TiO_3$ (BNT52) polycrystalline ceramic was prepared by the solid state reaction method and the details can be found elsewhere.[34] The fatigue experiment on bulk specimens was performed with bipolar triangular waveform electric fields at 4 Hz and 45 kV cm^{-1}. Crystal structure and electric properties were measured at a series of cycling intervals. For ferroelectric characterizations, silver films were sputtered to serve as electrodes. The polarization (*P*) versus electric field (*E*) hysteresis loops were measured using a standardized ferroelectric test system (RT-66A, Radiant Technologies) at 4 Hz at room temperature. The longitudinal strain (x_{33}) developed under electric field in the form of a triangular wave of 0.05 Hz was monitored with an MTI-2000 fotonic sensor (MTI Instruments Inc., Albany, NY). For X-ray diffraction measurements, the same bulk ceramic specimen for fatigue measurement was used. At each cycling interval, the silver film electrodes were chemically removed using dilute nitric acid solution. The evolution of the ½(311) superlattice peak was immediately recorded on a Siemens D500 diffractometer using Cu-Kα radiation at a 0.02° step size and a 150 s dwelling time. The integrated peak intensities were calculated with the baseline at $I = [I(37.80°) + I(38.65°)]/2$, where I is the X-ray photon count. For the electric field in situ TEM study, disk specimens (3 mm in diameter) were prepared from as-sintered pellets

through standard procedures including grinding, cutting, dimpling, and ion mill. The dimpled disks were annealed at 400 °C for 2 h to minimize the residual stresses before Ar-ion milling to the point of electron transparency. In situ TEM experiments were carried out on a specimen that was crack free at the edge of the central perforation on a Phillips CM30 microscope operated at 200 kV. Detailed experimental setup can be found in our previous reports.[28–31] For the in situ fatigue test in the TEM, bipolar electric fields in a triangular waveform at a frequency of 1 Hz and a nominal peak field of 30 kV cm^{-1} were applied. It should be pointed out that the TEM specimen has a central perforation which intensifies the actual field in the grain of interest. The intensification ratio depends primarily on the geometry of the perforation.[28,53] In the present work, this ratio is estimated to be close to 2. Only the nominal electric field (the applied voltage divided by the electrode spacing) is cited for the in situ TEM results in the text. TEM images were recorded at zero field after certain electric cycles were made.

Acknowledgements

The National Science Foundation (NSF), through Grant No. DMR-1037898, supported this work.

Received: August 11, 2014
Revised: October 22, 2014
Published online: November 11, 2014

[1] J. F. Scott, *Ferroelectric memories*, Springer, Berlin, **2000**.
[2] D. C. Lupascu, *Fatigue in ferroelectric ceramics and related issues*, Springer, Heidelberg, **2004**.
[3] N. Balke, M. Gajek, A. K. Tagantsev, L. W. Martin, Y.-H. Chu, R. Ramesh, S. V. Kalinin, *Adv. Funct. Mater.* **2010**, *20*, 3466.
[4] R. C. G. Naber, K. Asadi, P. W. M. Blom, D. M. de Leeuw, B. de Boer, *Adv. Mater.* **2010**, *22*, 933.
[5] V. Garcia, S. Fusil, K. Bouzehouane, S. Enouz-Vedrenne, N. D. Mathur, A. Barthélémy, M. Bibes, *Nature* **2009**, *460*, 81.
[6] M. A. Khan, U. S. Bhansali, M. N. Almadhoun, I. N. Odeh, D. Cha, H. N. Alshareef, *Adv. Funct. Mater.* **2014**, *24*, 1372.
[7] D. C. Lupascu, J. Rödel, *Adv. Eng. Mater.* **2005**, *7*, 882.
[8] A. K. Tagantsev, I. Stolichnov, E. L. Colla, N. Setter, *J. Appl. Phys.* **2001**, *90*, 1387.
[9] X. J. Lou, *J. Appl. Phys.* **2009**, *105*, 024101.
[10] S. Zhukov, Y. A. Genenko, O. Hirsch, J. Glaum, T. Granzow, H. V. Seggern, *Phys. Rew. B* **2010**, *82*, 014109.
[11] J. Glaum, M. Hoffman, *J. Am. Ceram. Soc.* **2014**, *97*, 665.
[12] P. K. Larsen, G. J. M. Dormans, D. J. Taylor, P. J. Veldhoven, *J. Appl. Phys.* **1994**, *76*, 2405.
[13] E. L. Colla, A. K. Tagantsev, D. V. Taylor, A. L. Kholkin, *Integr. Ferroelectr.* **1997**, *18*, 19.
[14] X. J. Lou, M. Zhang, S. A. T. Redfern, J. F. Scott, *Phys. Rev. Lett.* **2006**, *97*, 177601.
[15] J. F. Scott, C. A. Araujo, B. M. Melnick, L. D. McMillan, R. Zuleeg, *J. Appl. Phys.* **1991**, *70*, 382.
[16] W. L. Warren, D. Dimos, B. A. Tuttle, G. E. Pike, R. W. Schwartz, P. J. Clews, D. C. Mcintyre, *J. Appl. Phys.* **1995**, *77*, 6695.
[17] X. Zou, L. You, W. Chen, H. Ding, D. Wu, T. Wu, L. Chen, J. Wang, *ACS Nano* **2012**, *6*, 8997.
[18] S. M. Yang, T. H. Kim, J-G. Yoon, T. W. Noh, *Adv. Funct. Mater.* **2012**, *22*, 231.
[19] E. A. Patterson, D. P. Cann, *Appl. Phys. Lett.* **2012**, *101*, 042905.
[20] H. Z. Guo, S. J. Zhang, S. P. Beckman, X. Tan, *J. Appl. Phys.* **2013**, *114*, 154102.
[21] H. Z. Guo, C. Ma, X. M. Liu, X. Tan, *Appl. Phys. Lett.* **2013**, *102*, 092902.
[22] S-H. Baek, C. M. Folkman, J-W. Park, S. Lee, C-W. Bark, T. Tybell, C-B. Eom, *Adv. Mater.* **2011**, *23*, 1621.
[23] A. Gruverman, O. Auciello, H. Tokumoto, *Appl. Phys. Lett.* **1996**, *69*, 3191.
[24] S. Tsurekawa, H. Hatao, H. Takahashi, Y. Morizono, *Jpn. J. Appl. Phys.* **2011**, *50*, 09NC02.
[25] E. L. Colla, S. Hong, D. V. Taylor, A. K. Tagantsev, N. Setter, K. No, *Appl. Phys. Lett.* **1998**, *72*, 2763.
[26] E. L. Colla, I. Stolichnov, P. E. Bradely, N. Setter, *Appl. Phys. Lett.* **2003**, *82*, 1604.
[27] D-H. Do, P. G. Evans, E. D. Isaacs, D. M. Kim, C. B. Eom, E. M. Dufresne, *Nat. Mater.* **2004**, *3*, 365.
[28] X. Tan, H. He, J. K. Shang, *J. Mater. Res.* **2005**, *20*, 1641.
[29] H. He, X. Tan, *Phys. Rev. B* **2005**, *72*, 024102.
[30] X. Tan, J. K. Shang, *Philos. Mag. A* **2002**, *82*, 1463.
[31] H. Z. Guo, C. Zhou, X. Ren, X. Tan, *Phys. Rev. B* **2014**, *89*, 100104(R).
[32] Y. Sato, T. Hirayama, Y. Ikuhara, *Phys. Rev. Lett.* **2011**, *107*, 187601.
[33] Z. H. Zhang, X. Y. Qi, X. F. Duan, *Appl. Phys. Lett.* **2006**, *89*, 242905.
[34] X. M. Liu, H. Z. Guo, X. Tan, *J. Eur. Ceram. Soc.* **2014**, *34*, 2997.
[35] C. Ma, H. Z. Guo, S. P. Beckman, X. Tan, *Phys. Rev. Lett.* **2012**, *109*, 107602.
[36] A. M. Glazer, *Acta Cryst. A* **1975**, *31*, 756.
[37] D. I. Woodward, I. M. Reaney, *Acta Cryst. B* **2005**, *61*, 387.
[38] L. E. Cross, *Ferroelectrics* **1987**, *76*, 241.
[39] A. A. Bokov, Z.-G. Ye, *J. Mater. Sci.* **2006**, *41*, 31.
[40] H. Z. Guo, X. Liu, W. Hong, X. Tan, submitted, **2014**.
[41] S. Leoni, R. Ramlau, K. Meier, M. Schmidt, U. Schwarz, *Proc. Natl. Acad. Sci. U.S.A.* **2008**, *105*, 19612.
[42] V. Y. Shur, A. R. Akhmatkhanov, I. S. Baturin, *J. Appl. Phys.* **2012**, *111*, 124111.
[43] C. Brennan, *Ferroelectrics* **1993**, *150*, 199.
[44] Z. Luo, J. Glaum, T. Granzow, W. Jo, R. Dittmer, M. Hoffman, J. Rödel, *J. Am. Ceram. Soc.* **2011**, *94*, 529.
[45] F. Kubel, H. Schmid, *Acta Cryst. B* **1990**, *46*, 698.
[46] J. E. Daniels, T. R. Finlayson, M. Davis, D. Damjanovic, A. J. Studer, J. L. Jones, *J. Appl. Phys.* **2007**, *101*, 104108.
[47] W. Zhu, L. E. Cross, *Appl. Phys. Lett.* **2004**, *84*, 2388.
[48] C.-Y. Hsieh, Y.-F. Chen, W. Shih, Q. Zhu, W.-H. Shih, *Appl. Phys. Lett.* **2009**, *94*, 131101.
[49] W. Cao, *Ferroelectrics* **2003**, *290*, 107.
[50] Y. Kitanaka, K. Yanai, Y. Noguchi, M. Miyayama, Y. Kagawa, C. Moriyoshi, Y. Kuroiwa, *Phys. Rev. B* **2014**, *89*, 104104.
[51] H. Simons, J. Glaum, J. E. Daniels, A. J. Studer, A. Liess, J. Rödel, M. Hoffman, *J. Appl. Phys.* **2012**, *112*, 044101.
[52] J. Glaum, T. Granzow, L. A. Schmitt, H.-J. Kleebe, J. Rödel, *Acta Mater.* **2011**, *59*, 6083.
[53] R. M. McMeeking, *J. Appl. Math. Phys.* **1989**, *40*, 615.